Transformer Position Sensor for a Pneumatic Cylinder

Pavel Ripka, Mehran Mirzaei, Andrey Chirtsov and Jan Vyhnanek

Faculty of Electrical Engineering, Czech Technical University
Prague 16627, Czech Republic, e-mail: ripka@ fel.cvut.cz

Abstract—**A novel transformer-based sensor for a pneumatic cylinder enables measurements of the piston position to be made through a thick conductive cylinder. Unlike existing industrial solutions, which are mainly based on a moving magnet, our sensors do not require modifications to the parts inside the cylinder.**

Finite element analysis results are compared with measurements at various piston positions and excitation frequencies. Using a suitable model for the magnetic properties of the iron piston bar, we achieved good agreement between the model and reality.

When the sensor is operated at 100 Hz, the sensitivity is 200 mV/FS and the raw linearity error is 1.6% of the full 400 mm stroke.

Keywords— **Position sensor, transformer, pneumatic, cylinder**

I. INTRODUCTION

Sensing the position of a piston inside a pneumatic aluminium cylinder is a challenging task which is necessary for controlling the piston. The piston is shielded by the aluminium cylinder, which makes piston position measurements difficult. Various techniques are used for piston sensing transducers. Direct mounting of sensors inside the piston rod requires a gun-drilled long precise hole, which is expensive and may reduce the mechanical stability of the rod [1]. The use of microwave sensors on the piston is not reliable, and it is also mechanically complicated [2]. An optical scale [3] or a magnetic scale [4] on the piston rod allows only incremental position sensing. Using of magnetostrictive delay line principle is not suitable for harsh environment [5-7]. Remanent field of ferromagnetic piston was used in [8] for position measurement. This approach is not practical, as the remanent field changes with time and temperature and can also be significantly changed by external magnetic fields.

The method currently used by industry is external sensing of the piston position using a permanent magnet mounted on the piston with a non-magnetic stainless-steel rod. Permanent magnet fields are measured by an array of magnetic field sensors to detect the piston position. Although this method is robust and reliable, it requires a piston rod made of non-magnetic stainless steel, which is expensive. The authors recently developed an AC-excited contactless piston position transducer with axial excitation [9]. The field changes caused by a moving ferromagnetic piston rod are sensed by an array of integrated fluxgate sensors. While 0.1 mm resolution is achievable, the uncorrected maximum static error was ±3 mm. Limiting factor for this transducer is the dynamic performance: even at speed of 0.2 m/s the maximum dynamic error is ±3 mm. This type of sensor also requires complex signal processing of the sensor array. Similar results were obtained using radial excitation by saddle coils [10].

A much simpler solution is to evaluate the inductance of a solenoid coil around an aluminium cylinder and sensing piston. This type of sensor was developed by Sumali et al. [11], but only for cylinder made of non-conducting composite. Later simulations have shown that the linearity error of such sensor can be decreased by proper design of the coil [12]. We have experimentally verified the performance of a transducer of this kind even for the conducting cylinder within the industrial temperature range [13, 14]. However, the dynamic performance of a sensor based on measured inductance is problematical. Measuring the voltage induced into the secondary coil is a faster solution for dynamic position sensing of the piston. The transformer-based position transducer is a well-known solution [15 - 22]. One excitation coil and several pick-up coils are implemented in the transformer type of the position transducer. While the moving coil type [15], [18, 19] is not practical for our application, however, the conventional LVDT transducer, which uses a ferromagnetic core instead, is more suitable [16, 17]. Our aim was to adopt the LVDT principle for cases with a highly asymmetric core that moves inside the conducting cylinder.

In this paper, a transformer-based position sensor for a pneumatic cylinder with an aluminium shell, an aluminium piston and a ferromagnetic steel rod is analysed, designed and evaluated. A 2D axisymmetric finite element method (FEM) is used for the modelling. A frequency analysis with and without the iron rod and piston is performed in order to find proper operational conditions for the best precision. We also discuss how to read the secondary coils voltages to achieve the best sensor characteristics.

II. MODEL OF PNEUMATIC CYLINDER

Fig. 1 shows the pneumatic cylinder model at different

piston positions. Two sets of coils are used for the position sensor.
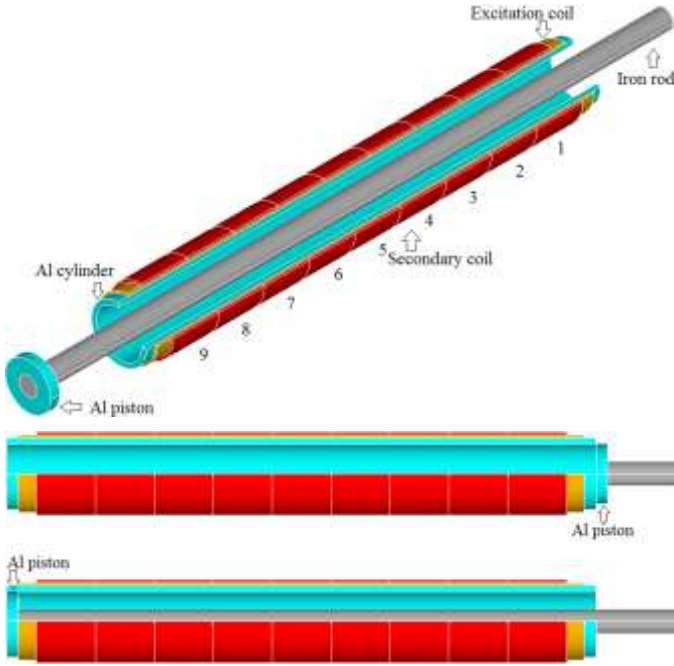

Fig. 1. A model of the transformer position sensor for a pneumatic cylinder – the full model (above), the axisymmetric model at the zero position of the piston (middle), and the axisymmetric model at the end position of the piston (below)

The model has an axisymmetric configuration, which reduces the model to a 2D configuration for the simulations. The first layer is the excitation coil, which is wound around the aluminium cylinder. The second layer coil is divided into 9 sections of pick-up coils.

Table I shows the dimensions of the pneumatic cylinder and the material data.

TABLE I. DIMENSIONS AND MATERIAL DATA

Parameter	Value
Cylinder outer diameter, D_{co}	60 (mm)
Cylinder inner diameter, D_{ci}	56 (mm)
Cylinder axial length, L_c	500 (mm)
Piston outer diameter, D_{po}	56 (mm)
Piston inner diameter, D_{pi}	20 (mm)
Piston axial length, L_p	10 (mm)
Iron rod diameter, D_i	20 (mm)
Iron rod axial length, L_i	700 (mm)
Number of turns for the excitation coil, N_e	800
Number of turns for each pick up coil, N_{pc}	77
Number of pick up coils, n_p	9
Wire diameter, D_w	0.56 (mm)
Aluminium electrical conductivity at 20ºC, σ_{Al}	30.5 (MS/m)
Iron electrical conductivity at 20 (ºC), σ_i	4.51 (MS/m)

III. MAGNETIC PROPERTIES OF THE IRON ROD

The correct relative magnetic permeability is important for FEM simulations and analysis. It is difficult to estimate the relative magnetic permeability of the iron rod, because the magnetic fields are low [13]. The relative magnetic permeability can therefore be considered as the initial permeability. Solid irons and steels have different initial permeability, depending on the chemical composition and the processing [23].

One method for finding the relative magnetic permeability is to use the excitation coil inductance. We measured this inductance for a fully-inserted rod, and we estimated the permeability iteratively using the FEM model. Fig. 2 shows the relative magnetic permeability versus the excitation current amplitude evaluated by this method. The relative magnetic permeability increases with increasing current, because the operating points are in the Rayleigh region of the B-H curve.

A second method for estimating the relative magnetic permeability for low fields is to extrapolate the B-H curve for small field values. In standard material models, the measured B-H curve is usually available only for fields above 50 mT [24]. The simplest method for estimating the relative magnetic permeability for lower fields is a simple line, which is calculated on the basis of the first two points from the measured B and H values. The simple equivalent line curve fitting function estimates initial permeability around 70 (Fig. 3). The estimated values from the B-H curve are compatible with the estimated value from the measured inductance, $\mu_r = 77.5$ (Fig. 2). The increasing relative magnetic permeability for a higher excitation coil current and higher magnetic field strength should be taken into account for precise simulations of a position sensor.

IV. OPERATION THEORY

A. Inductances of Air Core Solenoid coils

The magnetic vector potential of a finite-length solenoid coil is calculated as follows [25, 26] at a point with cylindrical coordinates r and z:

$$A_\varphi = \frac{\mu_0 \cdot N \cdot I \cdot r_w}{\pi} \cdot \int_{-0.5L_w}^{0.5L_w} \frac{\left(2-k_1^2\right) \cdot K(k_1^2) - 2 \cdot E(k_1^2)}{\beta \cdot k_1^2} dl$$
$$\alpha = \sqrt{r_w^2 + r^2 + (z+l)^2 - 2 \cdot r_w \cdot r}$$
$$\beta = \sqrt{r_w^2 + r^2 + (z+l)^2 + 2 \cdot r_w \cdot r} \qquad (1)$$
$$k_1 = \sqrt{1 - \frac{\alpha^2}{\beta^2}}$$

where, μ_0 is the permeability of the open space, N is the number of turns of the solenoid coil, I is the current, r_w is the mean radius of the solenoid coil, L_w is coil length, K are the complete elliptic integrals of the first kind, and E are the complete elliptic integrals of the second kind.

Fig. 4 shows the magnetic flux distribution for various finite length solenoid coils. The end effects are more visible in a shorter coil, which changes the inductance considerably, than when an infinite length solenoid coil is used.

The self inductance of the air core solenoid coil L, and of the induced voltage U are as follows with negligible wires diameters:

$$U = L \cdot \frac{dI}{dt}, \quad L = C \cdot \frac{N^2}{\Re}, \quad \Re = \frac{L_w}{\mu_0 \cdot \pi \cdot r_w^2} \tag{2}$$

where C is the end effect factor caused by the finite length of the solenoid coil. Parameter C is equal to 1 for a solenoid coil of infinite length. Parameter C can be computed [27] using the exact formula in (3) or using the approximate formula in (4):

$$C = \frac{8}{3 \cdot \pi} \cdot \frac{r_w}{L_w} \cdot \left(\frac{1 - k_2^2}{k_2^3} \cdot K\left(k_2^2\right) + \frac{2k_2^2 - 1}{k_2^3} \cdot E\left(k_2^2\right) - 1 \right)$$

$$k_2 = \sqrt{\frac{\left(\frac{r_w}{L_w}\right)^2}{\sqrt{\left(\frac{r_w}{L_w}\right)^2 + 0.25}}} \tag{3}$$

$$C = 1 - \frac{8}{3 \cdot \pi} \cdot \frac{r_w}{L_w} \tag{4}$$
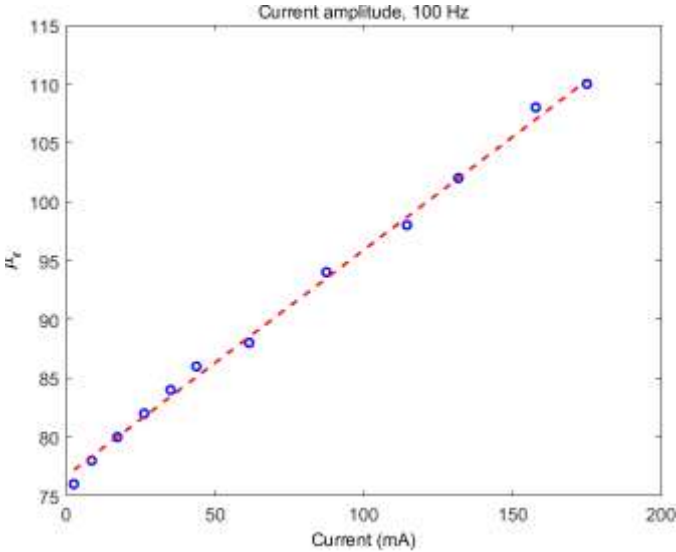
Fig. 2. Relative magnetic permeability, μ_r-I_m curve when the piston is in the end position - (estimated from the inductance [13])
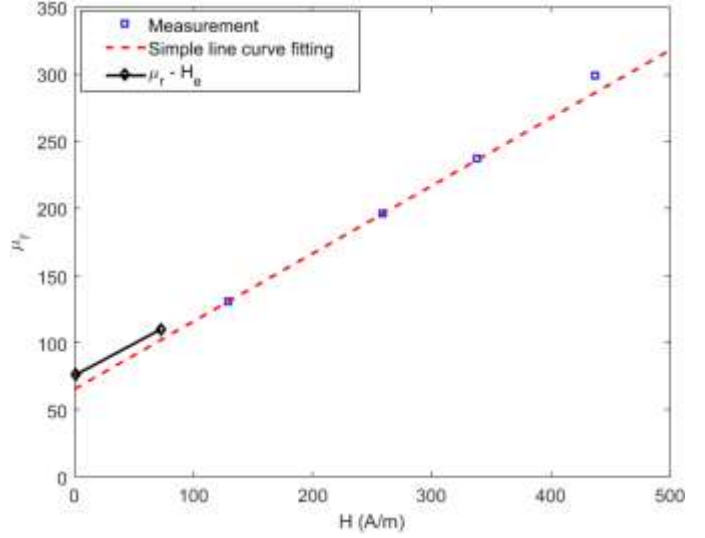
Fig. 3. Relative magnetic permeability, the μ_r-H curve - measured from yoke, and μ_r-H_e, calculated from Fig. 2 (H_e is effective H on the surface of the iron rod)
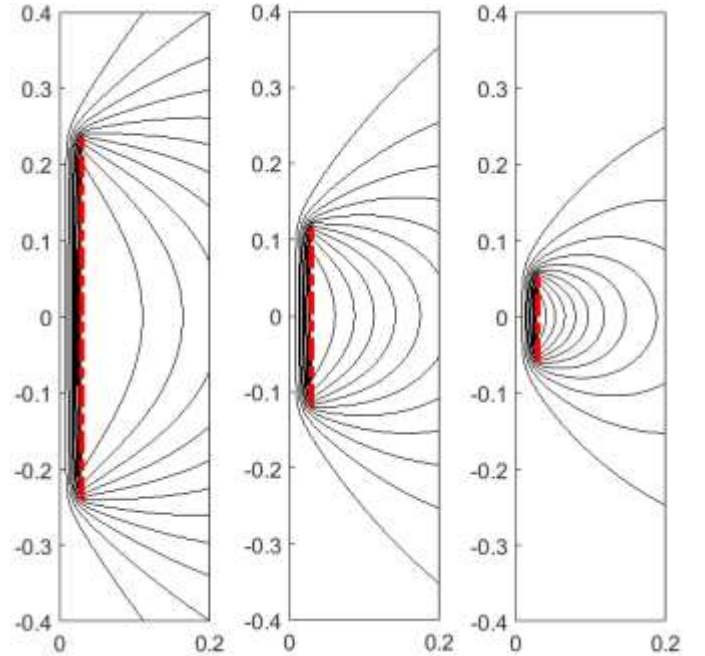

Fig. 4. Magnetic flux distribution in a solenoidal coil (the red dashed line shows the solenoid coil) using (1), which depicted sizes are in meter unit - solenoid length 480 mm (left), solenoid length 240 mm (middle), and solenoid length 120 mm (right) with coil radius 30 mm

The resulting mutual inductance between the excitation coil with axial length, L_{ew} and the pick up coil with axial length L_{pw} (Fig. 1) and induced voltage U_m can be presented as follows:

$$U_m = M \cdot \frac{dI}{dt}, \quad M = C \cdot \frac{N_e \cdot N_p}{\Re} = \frac{N_p}{N_e} \cdot L \tag{5}$$

where, N_e (=800) is the number of turns for the exciting coil, and N_p ($n_e \cdot N_{pc} = 693$), is the number of turns for the pick-up coil. For simplicity, the effects of the wires diameters are neglected when computing (3) - (5) as the wires diameters are

3

very small in comparison with coil radius.

Table II shows parameter C for various solenoid coil lengths. It decreases with decreasing coil length, L_{ew}. The smaller r_w/L_{ew} ratio causes the smaller field end effects of a solenoid coil of finite length.

TABLE II
FIELD END EFFECT C

L_{ew} (mm)	C - using (3)	C - using (4)
480	0.949	0.947
240	0.902	0.894
120	0.818	0.788

B. Real Inductances

A conductive aluminium cylinder and piston and a conductive solid iron rod cause a change in the self-inductance of the exciting coil, and also mutual inductance between the exciting coil and the pick-up coil, because of the induced eddy currents in the solid parts and the high permeability of iron.

A 2D axisymmetric finite element method is used to calculate the self-inductance and the mutual inductance, taking into account the solid aluminium cylinder and the solid iron rod [24]. Equations (6) and (7) present the governing equations extracted from the Maxwell equations for a 2D axisymmetric model [25]. The first term of (7) is for the excitation coil region, and the second term is for the solid conductive parts of the cylinder and the iron rod (Fig. 1).

$$
\begin{aligned}
&B_r = \mu \cdot H_r, B_z = \mu \cdot H_z \\
&\frac{1}{r}\frac{\partial}{\partial r}\left(r\frac{\partial A_\varphi}{\partial r}\right) - \frac{A_\varphi}{r^2} + \frac{\partial^2 A_\varphi}{\partial z^2} = -\mu \cdot J_\varphi \\
&B_r = -\frac{\partial A_\varphi}{\partial z}, B_z = \frac{1}{r}\frac{\partial(rA_\varphi)}{\partial r}
\end{aligned}
\tag{6}
$$

$$
\begin{aligned}
&J_\varphi = J_s \\
&J_\varphi = -\sigma\frac{\partial A_\varphi}{\partial t} = -j\omega\sigma A_\varphi, \quad \omega = 2\pi f
\end{aligned}
\tag{7}
$$

where, B_r is the radial component of the magnetic flux density, H_r is the radial component of the magnetic field strength, B_z is the axial component of the magnetic flux density, H_z is the axial component of the magnetic field strength, μ is the relative magnetic permeability, A_φ is the magnetic vector potential, J_φ is the azimuthal-angle component of the current density, J_s is the source current density (excitation coil), and σ is the electrical conductivity of the solid parts (the aluminium cylinder and the iron rod). f is electrical frequency.

Fig. 5 shows the magnetic flux distribution with and without an iron rod and an aluminium cylinder, calculated by FEM. It is clear that the conductive parts have a significant influence on the distribution of the magnetic flux. The self-inductance of the exciting coil and the mutual inductance are shown in Fig. 6 - Fig 8. The ratio between self inductance and mutual inductance in Fig. 6 - Fig. 8 follows the correspondence in (5), which is related to the number of turns of the exciting coil N_e

and the pick-up coil N_p.

The self inductances at low frequencies in Fig. 6 are 4.7 mH for an infinite solenoid and 4.5 mH for a finite solenoid coil, which correspond to (2) - (4). The inductances decrease due to the skin effect in the conductive parts at higher frequencies f. A stronger skin effect reduces the effective area for magnetic flux inside the solenoid coil, which results in decreased self-inductances and mutual inductances.

The aluminium cylinder has a dominant effect on the inductances in the high frequency range above 100 Hz, compare Figs. 6 - 8. The resistive part is caused mainly by the induced eddy currents in the conductive parts of the iron rod and the aluminium cylinder. The curves for parameters $L·f$ and $M·f$ in Fig. 6 - Fig. 8 are proportional to the induced voltages in the excitation coil and in the secondary coil. Local maxima occur at about 100 Hz - 200 Hz in Fig. 6 and at 10 Hz in Fig. 7. In Fig. 8, parameters $L·f$ and $M·f$ versus frequency increase continuously until 1000 Hz. This shows that the eddy currents in the cylinder have a stronger effect than the eddy currents in the piston rod.

Fig. 9 shows the equivalent circuit of a pneumatic cylinder with an open secondary transformer model. Inductance L_o represents the standard equivalent circuit components in parallel connection related to the total magnetic energy, and resistance R_o represents the standard equivalent circuit components in parallel connection related to the total eddy current losses. The hysteresis losses are neglected, because the magnetic fields in the iron are very small. The excitation coil resistance is 13.7 Ω. Resistance R_o is very large when the eddy current losses and the coil resistance are negligible – this is true only at very low frequencies. Inductance L_o changes dramatically from 4.5 mH to 34 mH when the ferromagnetic rod is inserted – compare Fig. 7 with Fig. 6.
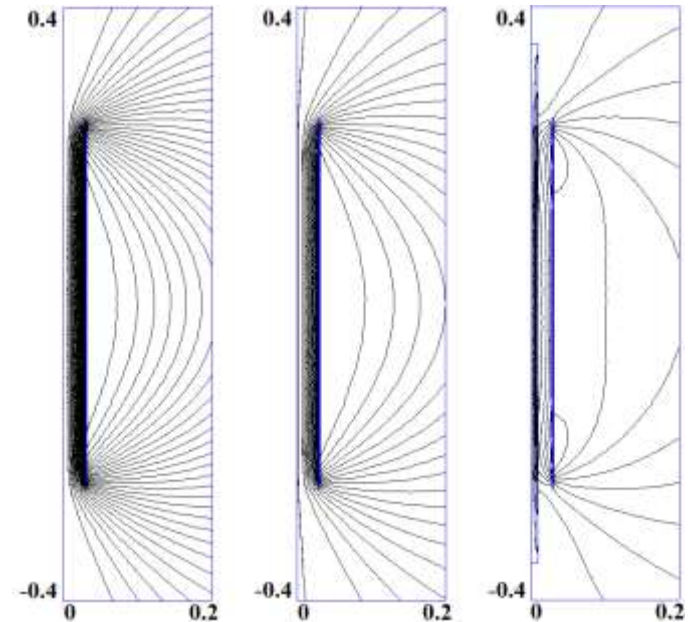

Fig. 5. Magnetic flux distribution using FEM at 100 Hz in a solenoidal coil without an iron rod and without an aluminium cylinder (left), with only an

aluminum cylinder (centre), and with an iron rod and with an aluminium cylinder - solenoid length 480 mm with a coil radius of 30 mm
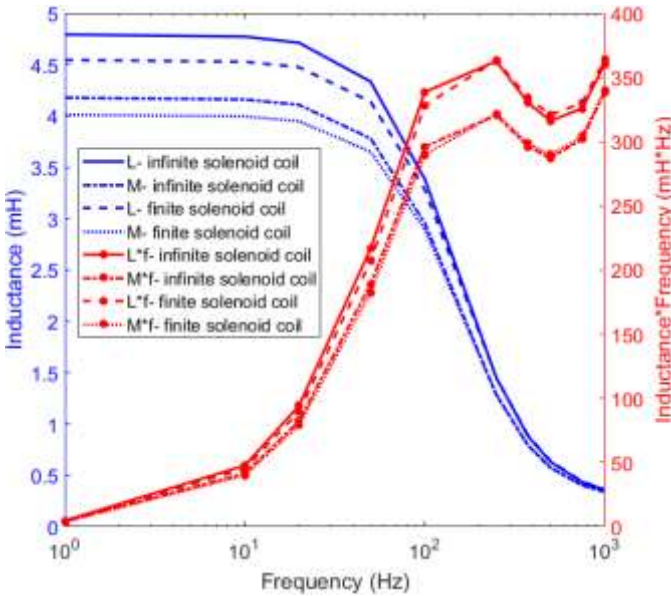

Fig. 6. Inductance versus frequency using FEM - with an aluminium cylinder and without an iron rod - solenoid coil length 480 mm
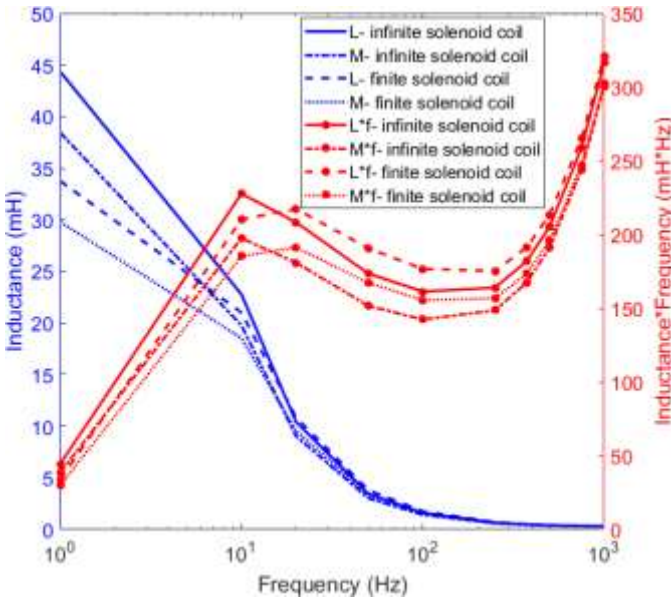

Fig. 7. Inductance versus frequency, using FEM - with an aluminum cylinder and with an iron rod - solenoid coil length 480 mm (μ_r= 77.5)
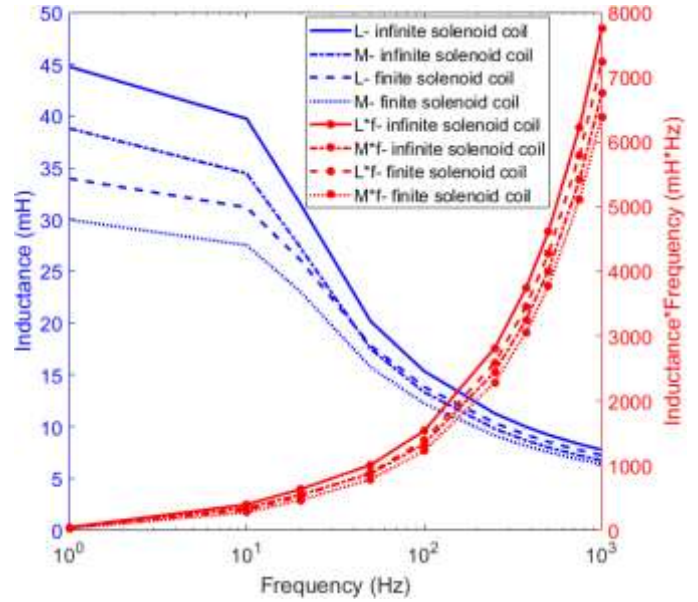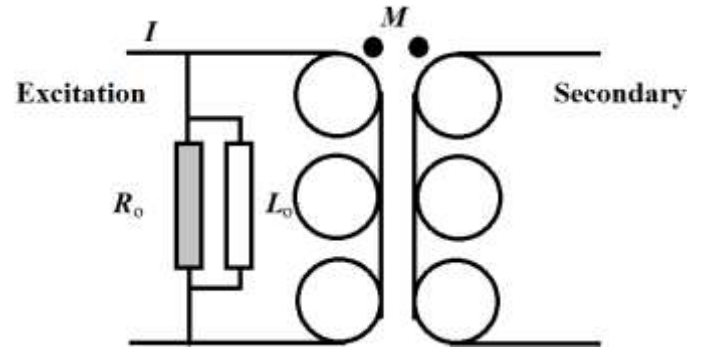

Fig. 8. Inductance versus frequency, using FEM - without an aluminum cylinder and with an iron rod - solenoid coil length 480 mm (μ_r= 77.5)

Fig. 9. Equivalent circuit for a pneumatic cylinder with the transformer model – the excitation coil is in the primary side

All measured and calculated inductances L in this paper are for series connection. However the equivalent circuit corresponding to core losses (Ro) and magnetic energy (Lo) for transformer is usually shown in parallel connection. The components in the equivalent series connections, *L* and *R*, are calculated:

$$L = \frac{R_o^2}{\omega^2 \, L_o^2 + R_o^2} \cdot L_o$$

$$R = \frac{\omega^2 \, L_o^2}{\omega^2 \, L_o^2 + R_o^2} \cdot R_o \qquad (8)$$

The first term concerning inductances is shown in Fig. 6 - Fig. 8. It is obvious that inductance *L* always decreases versus frequency.

Equation (9) shows the excitation coil induced voltage, V_e and the secondary or pick-up coil induced voltage, V_p. The induced voltages have real parts ($V_{e\text{-}r}$ and $V_{p\text{-}r}$) and imaginary parts ($V_{e\text{-}i}$ and $V_{p\text{-}i}$) referred to applied current *I* as a reference.

$$V_e = (R + j\omega L)\cdot I,\ V_{e-r} = R\cdot I,\ V_{e-i} = \omega L\cdot I$$

$$V_p = \frac{N_p}{N_e}V_e,\ V_{p-r} = \frac{N_p}{N_e}R\cdot I,\ V_{p-i} = \frac{N_p}{N_e}\omega L\cdot I \quad (9)$$

C. Inductances versus Iron Rod and Piston Position

Fig. 10 presents the inductances versus the position of the iron rod, without an aluminium cylinder, and Fig. 11 presents the inductances versus the position of the iron rod, with an aluminium cylinder. The inductances increase at DC and AC with greater penetration of the iron rod inside the solenoid coil without an aluminium cylinder, because the magnetic flux reluctance decreases as the high-permeability iron rod penetrates further inside the solenoid coil. The reverse occurs when an aluminium cylinder is added to the model, due to the high reaction fields of the induced eddy currents in the aluminium cylinder shell and the lower resistance R_o in (8) and the lower corresponding equivalent inductance L.
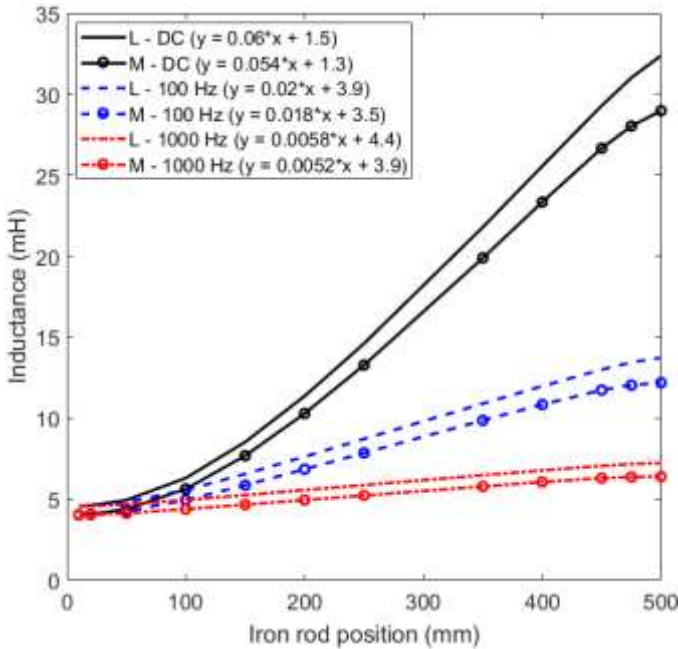
Fig. 10. Inductance versus iron rod position using FEM (with a linear curve fit equation) - without an aluminum cylinder - solenoid coil length 480 mm - μ_r= 77.5
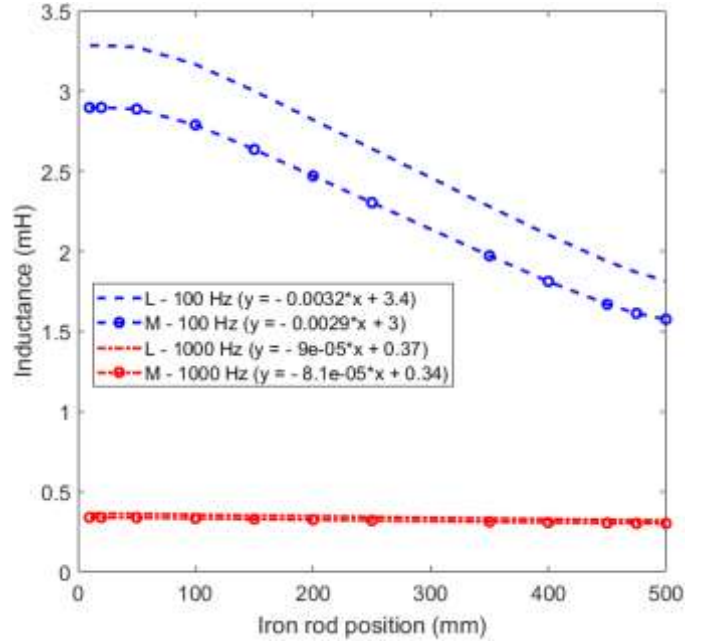

Fig. 11. Inductance versus iron rod position using FEM (with a linear curve fit equation) - with an aluminum cylinder - solenoid coil length 480 mm- μ_r= 77.5

Fig. 12. Measurement set-up for a pneumatic position sensor

V. EXPERIMENTAL RESULTS

Fig. 12 shows the experimental set-up for a pneumatic position sensor. A reference position sensor is used, which is connected to the iron rod. All the design data of the position sensor are presented in Table I [13]. We used a Senpos MRTM500 potentiometric linear position sensor with a measurement range of 500 mm and a linearity error of 0.05%. Lock-in amplifier is used for the measurement of the output voltage of our sensor. The power supply for excitation coil is a Keithley 3390 signal generator with internal impedance 50 Ω.

The magnetic field strength distributions in the pneumatic cylinder for various positions of the iron rod and the piston are presented in Fig. 13 at 100 Hz and at exciting current amplitude of 116 mA. The magnetic fields are higher in the model with the piston at the beginning of the cylinder, which causes higher magnetic energy in the system and higher self-inductance and mutual inductance than when the piston and the iron rod are at the end of the pneumatic cylinder.

The current of the exciting coil decreases slightly with increasing piston position and iron rod position (Fig. 14). The total impedance of the exciting coil increases, as shown in the

6

circuit in Fig. 14. The voltage source with amplitude of 10 V is in series with 70 Ω resistances, which causes small changes in the current with the position of the iron rod and the piston.
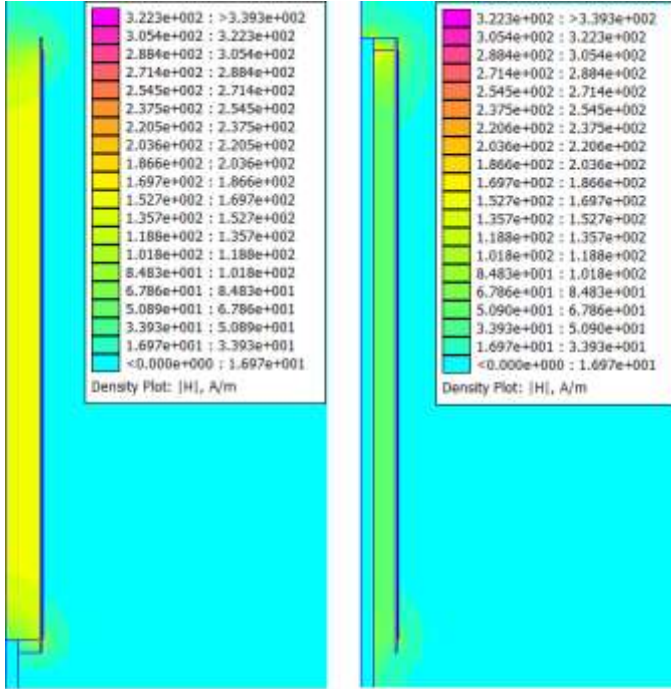

Fig. 13. Magnetic field strength distribution using FEM [24] at 100 Hz for the piston at the begining of the cylinder (left) and for the piston at the end of the cylinder (right) - μ_r= 100
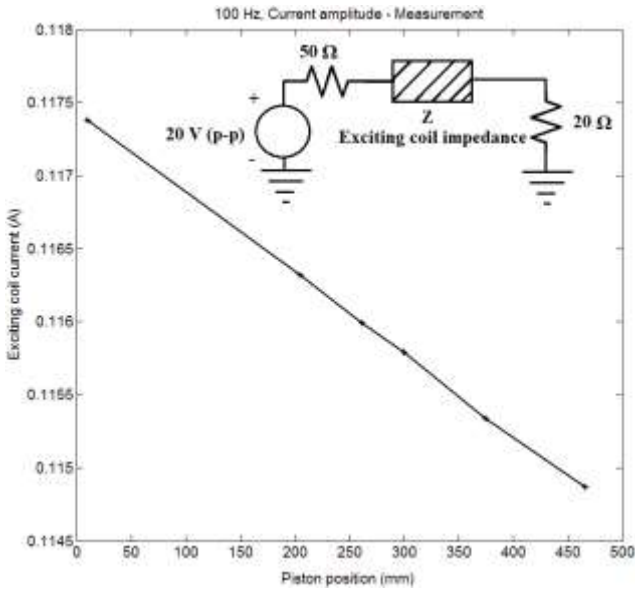

Fig. 14. Measured current of the excitation coil versus piston position, with schematics of the excitation circuit - the resistance of 20 Ω is for the current measurement

A. *Secondary voltage versus the position of the piston and the iron rod*

Figs. 15 - 17 show the experimental and FEM results for the secondary coils-induced voltage. The change in the current with the position of the piston is taken into consideration in the simulations. The FEM results for the induced voltages coincide well with the measurements. The relative permeability μ_r is considered to be equal to 100 (Fig. 2 and Fig. 3) in the simulations, based on the exciting current in Fig. 14.

The real part and the imaginary part of the secondary coil-induced voltage change almost linearly with the position of the piston in Fig. 17, which can be considered as a position meter for the pneumatic cylinder. The curve fit linear function for iron rod position X versus induced voltage V is presented in (10):

$$X = X_0 + K \cdot V \tag{10}$$

The constant X_0 (mm) and the constant K (mm/mV) are presented in Fig. 18 for 400 mm stroke. The root mean square error (RMSE) values as an indicator [11] for showing the closeness for 11 measured values to the curve fit linear function in (10) are 5.03 mm for the real part of the voltage and 6.31 mm for the imaginary part of voltage. The real part of the induced voltage shows more linear characteristics than the imaginary part of the induced voltage, based on RMSE.

Another indication for linearity of the position sensor is the correlation coefficient R^2. It is 0.9984 for the real part of the voltage and 0.9974 for the imaginary part of the voltage, which shows that the real part of the voltage is a more linear curve. Fig. 19 shows position errors versus piston position

The sensor characteristics deviate from linear at both ends of the cylinder. This can be partly compensated by increasing the number of turns for the peripheral coil sections or via calibration, but it should be noted that, for real pneumatic cylinders, the piston stroke is always shorter than the cylinder length. We therefore evaluate linearity error for 400 mm stroke.

B. *Secondary voltage versus frequency*

The excitation coil current changes with frequency (Fig. 20) because of the increase in coil impedance at higher frequencies.
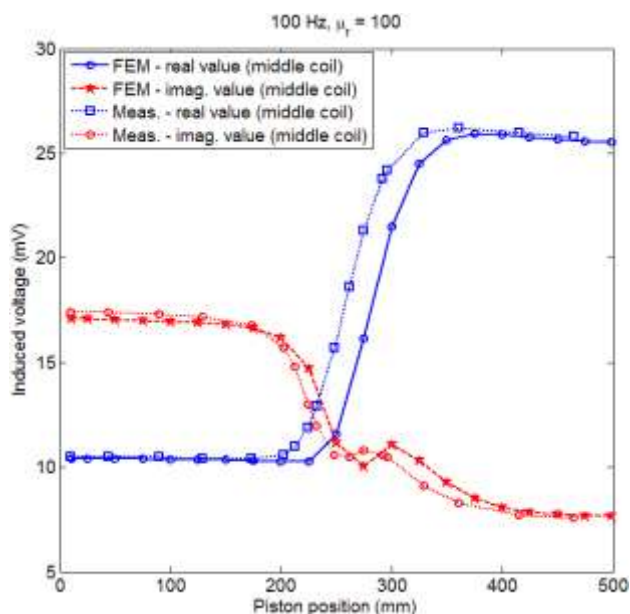
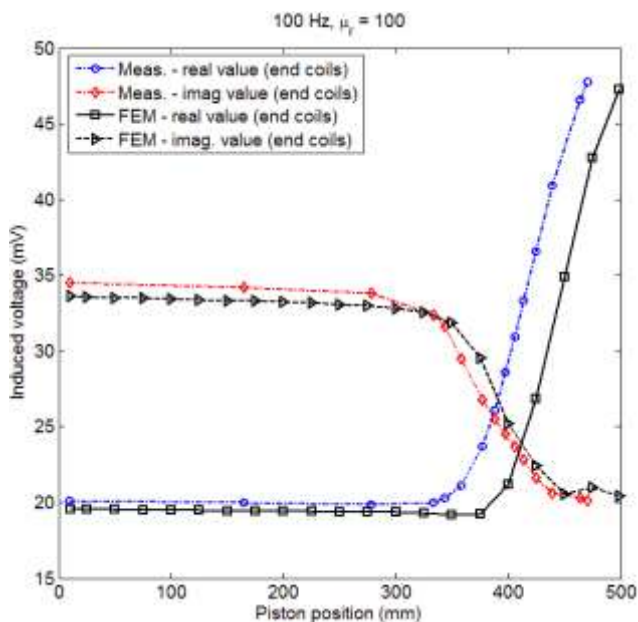Fig. 15. Induced voltages for secondary coil number 5 - middle coil

Fig. 16. Induced voltages for secondary coils numbers 8 and 9 in series (end coils)
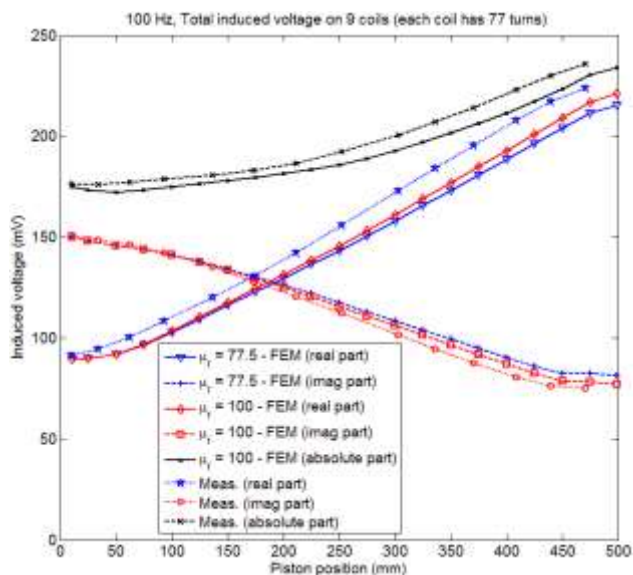
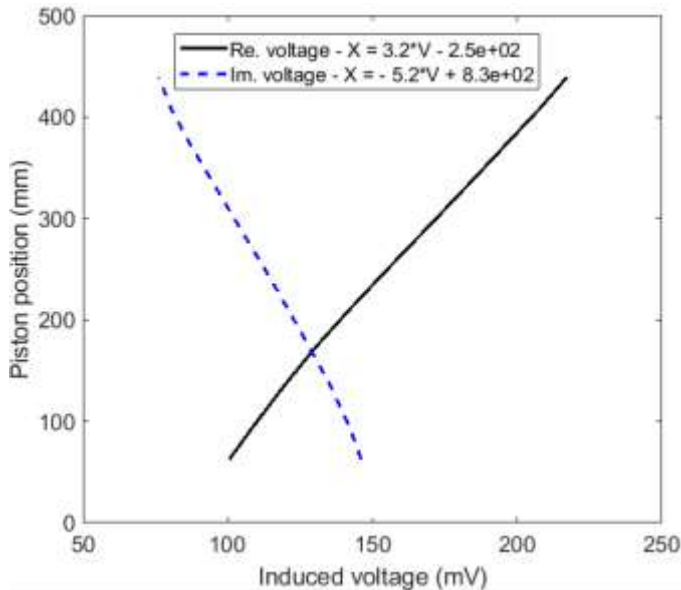Fig. 17. Induced voltages for all secondary coils connected serially

The secondary induced voltages at various excitation coil frequencies are shown in Fig. 21 - Fig. 23. The changes in current with frequency are taken into account in the simulations.

The results for different frequencies without an iron rod and with a fully-inserted iron rod and piston in the cylinder show the sensitivity of the position sensor versus frequency.

For the real part, the sensitivity maximum is 150 mV at 100 Hz and the sensitivity decreases rapidly at higher frequencies. However, the maximum sensitivity for the imaginary part is 100 mV at 200 Hz and at higher frequencies it may therefore be preferable to use the imaginary part of the induced voltage for fast moving cylinders.

Fig. 18. Piston position versus induced voltage and corresponding curve fit line functions

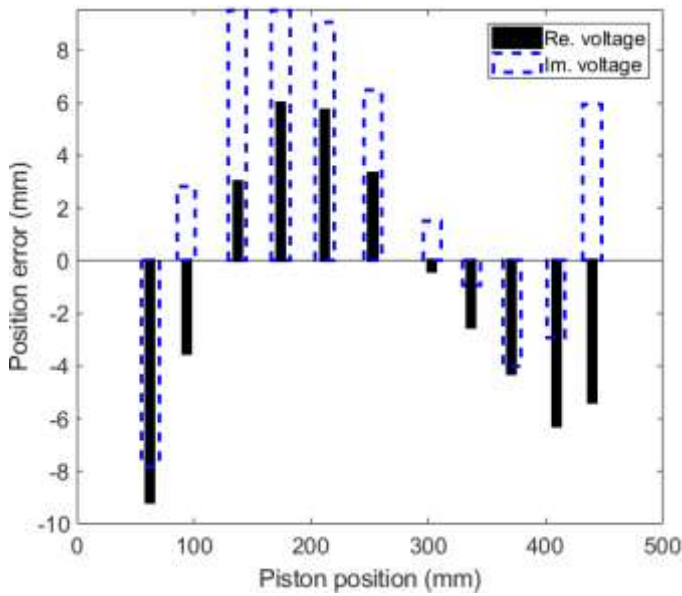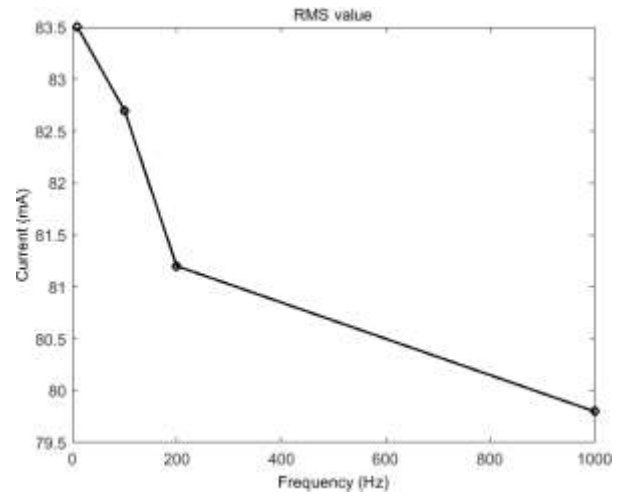Fig. 19. Position error versus piston position

Fig. 20. Measured current of the excitation coil versus frequency – the piston position is at the end of the cylinder
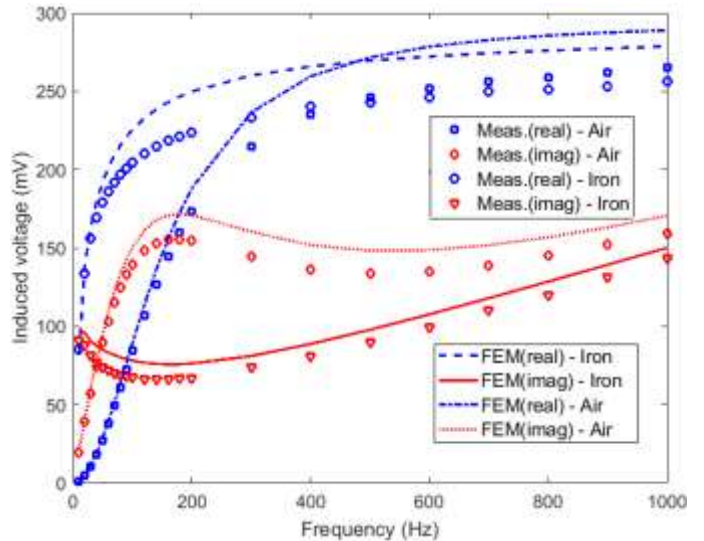

Fig. 21. Induced voltage for the full secondary coil with and without a piston iron rod - Air means without an iron rod, and iron means with a fully-inserted iron rod

The amplitude and the phase of the induced current in the aluminium cylinder are shown in Fig. 24 and Fig. 25. The phase angle without an iron rod (air) is about 90 deg. (Fig. 25) at low frequency, 10 Hz, which shows negligible resistance of the aluminium cylinder at a low frequency. The same phenomenon is shown in Fig. 22 with an inserted iron rod: the ferromagnetic material of the rod causes a phase shift even at small frequencies. The imaginary part of the induced current without an iron rod (Air) in Fig. 24 shows a maximum absolute value similar to Fig. 21 at about 190 Hz. From the measurements and simulations shown in Fig. 23, we can identify two prospective working frequencies for the position sensor: for the real part of the induced voltage, maximum sensitivity is around 80 Hz, and for the imaginary part the sensitivity maximum is at 190 Hz. The secondary induced voltage is therefore also recalculated at 190 Hz, see Fig. 26. The difference between the maximum voltage and the minimum voltage (imaginary parts) are higher at 190 Hz than at 100 Hz, which means higher sensitivity to piston position or less source power consumption at the same sensitivity as 100 Hz. To improve the dynamic performance, the excitation frequency can be raised to 400 Hz.

VI. IRON PERMEABILITY EFFECT

Fig. 27 and Fig. 28 show the excitation coil inductance and the secondary coil induced voltages versus the iron permeability. The negative slope is caused by the aluminium shell, and corresponds with the results shown in Fig. 11 and discussed in section IV. It is clear that iron permeability has a high impact on the position sensor outputs. It has to be measured, as various magnetic irons and magnetic steels could be used for the piston iron rod [23].
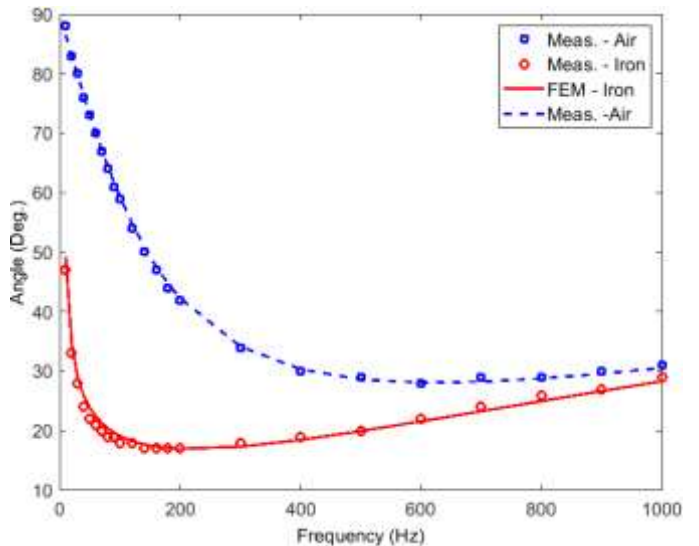
Fig. 22. Phase angle of the induced voltage for the full secondary coil with and without a piston iron rod
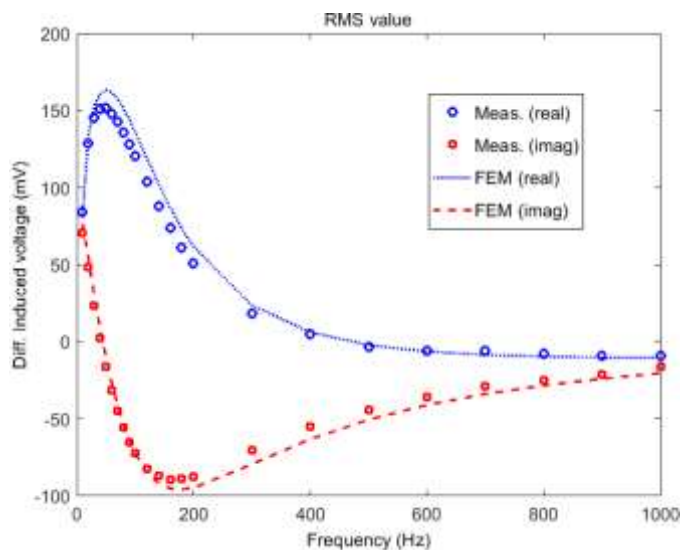

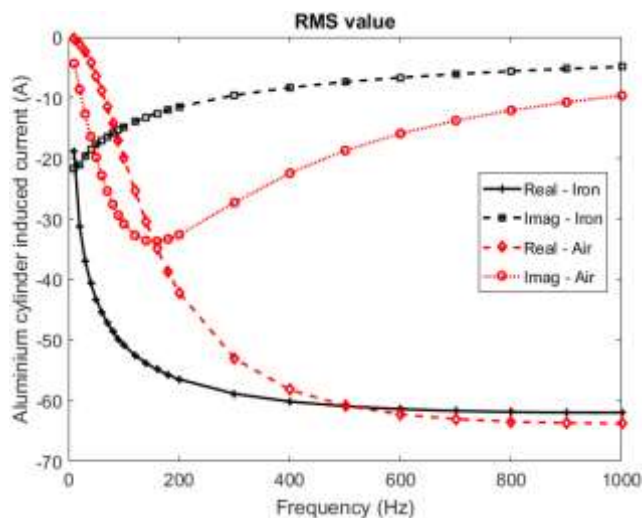Fig. 23. Difference in induced voltage between two extreme positions of the piston

Fig. 24. The induced eddy current in the aluminium cylinder with and without an iron rod
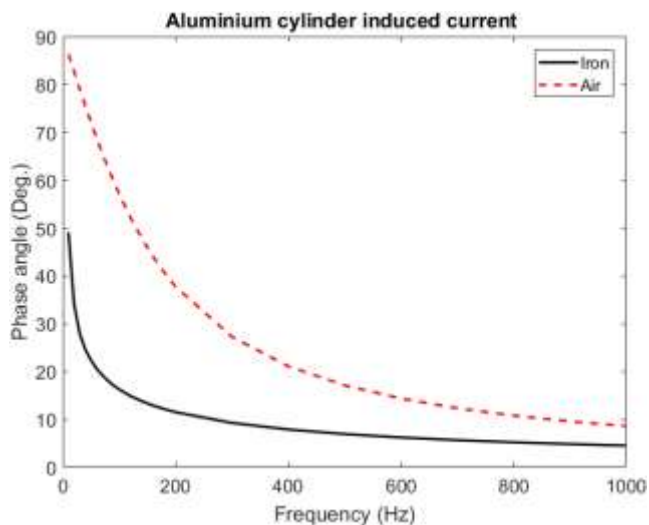

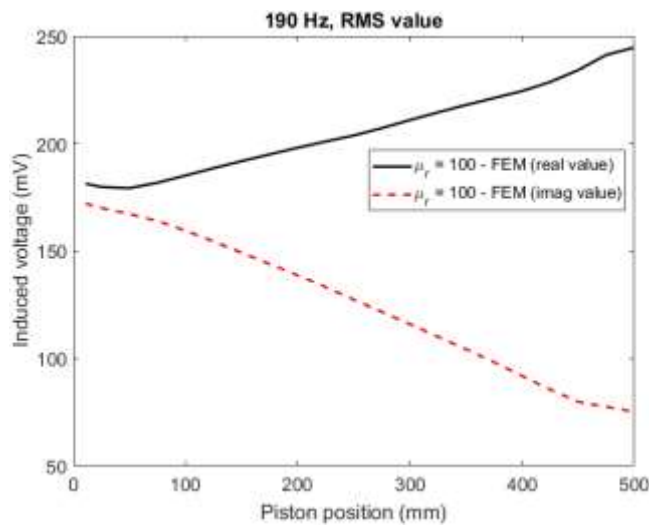Fig. 25. Phase angle of the induced current in the aluminium cylinder

Fig. 26. Induced voltages for a full secondary coil at 190 Hz (FEM simulation)
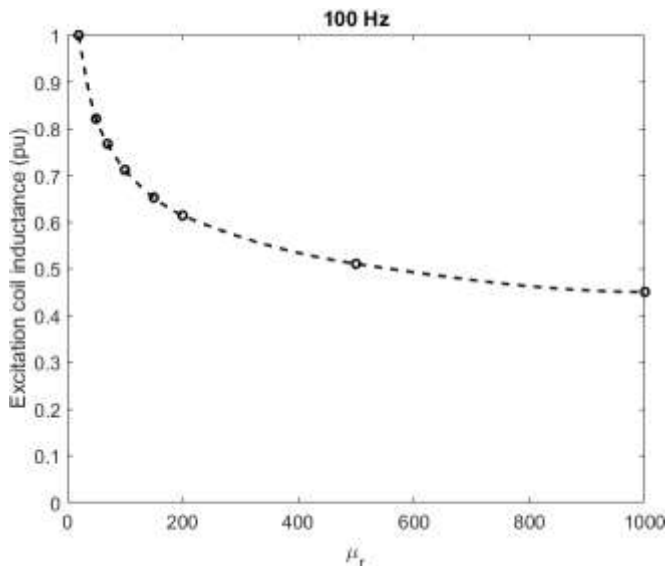
Fig. 27. Excitation coil inductance for various iron rod permeabilities – the piston position is at cylinder end position
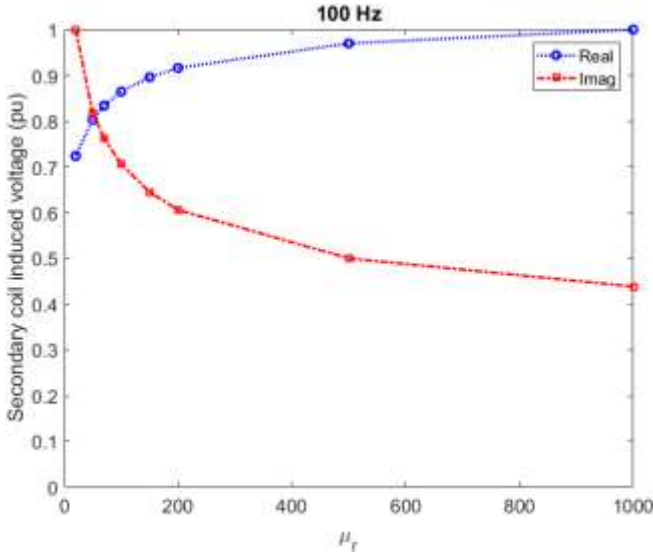

Fig. 28. Induced voltages for a full secondary coil for various iron rod permeabilities – the piston position is at cylinder end position
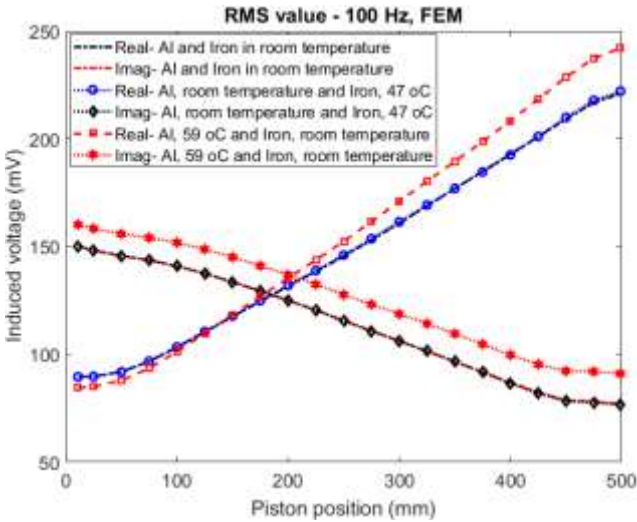

Fig. 29. Induced voltages for a full secondary coil at various iron and alumium temperatures (μ_r = 100)- the excitation frequency was 100 Hz.

VII. TEMPERATURE DEPENDENCY

Fig. 29 shows temperature effects on the induced voltage in the secondary coil. The electrical conductivity temperature dependency coefficient for iron, c_i and for aluminium, c_{Al} are as follows:

$$\sigma_i(\theta\,^oC) = \sigma_i(20\,^oC)\,/(1 + c_i \cdot (\theta - 20))$$
$$\sigma_i(20\,^oC) = 4.509\,MS/m \quad, \quad c_i = 0.0027356 \qquad (11)$$
$$\sigma_{Al}(\theta\,^oC) = \sigma_{Al}(20\,^oC) \cdot (1 + c_{Al} \cdot (\theta - 20))$$
$$\sigma_{Al}(20\,^oC) = 30.5\,MS/m \quad, \quad c_{Al} = 0.0041$$

where σ is electrical conductivity.

It is shown that an increase in the temperature of the iron rod has a negligible effect on the induced voltage, but the temperature of the aluminium changes the induced voltage of the secondary coil considerably. The imaginary part of the induced voltage increases 6% - 10% for a higher temperature of aluminium cylinder. This is similar to the change in the exciting coil inductance reported in [13]. The effect of temperature on iron rod permeability is negligible [14].

VIII. CONCLUSIONS

FEM modelling and experimental results for a transformer position sensor for a pneumatic cylinder have been presented. The results show the feasibility of using the principle of a linear transformer with a moving core for measuring the position of the piston in a pneumatic cylinder. Compared to conventional LVDT, our sensor has a highly asymmetric core which moves inside the conducting cylinder.

The sound match between FEM results and measurements shows that FEM can be used for optimizing a position sensor of this type.

The linearity rms error is maximum 1.6% of the full 400 mm stroke without any compensation..

The temperature sensitivity of the secondary coil voltage has been calculated for various iron and aluminium temperatures. The effect of the change in the electrical resistivity of an aluminium cylinder is clearly dominant at 100 Hz excitation frequency. Temperature compensation can be clearly made by using the voltage across the excitation coil. However, this topic lies beyond the scope of the present paper.

Using only fixed copper coils for excitation and pick up make the proposed position sensor for pneumatic cylinder more cost effective than position sensor using rare earth NdFeB permanent magnets and an array of Hall sensors. In industrial applications, single-chip synchronous detector such as AD630 can be used for the output voltage processing. Due to its simplicity the proposed position sensor is suitable for harsh environment such as high temperature and vibrations.

References

[1] Herceg, "Taking a position on hydraulic cylinder sensors," *Hydraulics & Pneumatics* 24–27 (2015).

[2] S. Fericean, A. Hiller-Brod, A. D. Dorneich, and M. Fritton, "Microwave displacement sensor for hydraulic devices," *IEEE Sensors Journal* 13(12) (2013), pp. 4682 - 4689

[3] A. A. M. Faudzi, K. Suzumori, and S. Wakimoto, "Design and control of new intelligent pneumatic cylinder for intelligent chair tool application," 2009 *IEEE/ASME International Conference on Advanced Intelligent Mechatronics*, Singapore, 2009, pp. 1909–1914.

[4] S. Y. Yang, M. C. Lee, M. H. Lee, and S. Arimoto, "Measuring system for development of stroke-sensing cylinder for automatic excavator," *IEEE Transactions on Industrial Electronics* 45(3), 376–384 (1998).

[5] E. Hristoforou, "Magnetostrictive delay lines and their applications," *Sensors and Actuators A-physical* , 59, 183–191 (1997).

[6] E. Hristoforou, P. D. Dimitropoulos, and J. Petrou, "A new position sensor based on the MDL technique," *Sensors and Actuators A-physical* 132, 112–121 (2006).

[7] Y. Wang, R. Madson, and R. Rajamani, "Nonlinear observer design for a magnetic position estimation technique," 2015 54th *IEEE Conference on Decision and Control* (CDC), Osaka, 2015, pp. 6986–6991.

[8] S. Taghvaeeyan, R. Rajamani, and Z. Sun, "Non-intrusive piston position measurement system using magnetic field," *IEEE Sensors Journal* 13(8), 3106–3114 (2013).

[9] P. Ripka, A. Chirtsov and V. Grim, "Contactless Piston Position Transducer With Axial Excitation", *IEEE Trans. on Magnetics*, : 2017, vol. 53, Issue: 11, 4002504

[10] J. Vyhnanek ,P. Ripka, and A. Chirtsov, "Linear position sensing through conductive wall without permanent magnet," *Proceedings* 2017, 1(4), 390

[11] H. Sumali ; E.P. Bystrom ; G.W. Krutz, "A displacement sensor for nonmetallic hydraulic cylinders," *IEEE Sensors Journal*, 2003, Volume: 3 , Issue: 6 pp. 818 - 826

[12] Seung-Ho Yang, K. Hirata, T. Ota, and Y. Kawase, "Impedance Linearity of Contactless Magnetic-Type Position Sensor," *IEEE Trans. on Magnetics*, Vol. 53, No. 6, June 2017 8001204

[13] P. Ripka, A. Chirtsov, and M. Mirzaei, "Inductance position sensor for pneumatic cylinder", *AIP Advances*, 8, 2018, 048001

[14] M. Mirzaei, P. Ripka, A. Chirtsov, and J. Vyhnanek, "Temperature influence on position transducer for pneumatic cylinder", *IEEE Sensors Conference* 2018, India paper #1638

[15] Y. Kano, S. Hasebe, C. Huang, T. Yamada, "New type linear variable differential transformer position transducer", *IEEE Trans. on Instrum. and Meas.*, Year: 1989, Volume: 38, Pages: 407 - 409

[16] M. Kilani, S. Taifour and L. Al-Sharif, "Effect of design geometry on the performance characteristics of linear variable differential transformers," *Sensors & Transducers*, Vol. 150, Issue 3, March 2013, pp. 66-71

[17] J. K. Sykulski, E. Sykulska, and S. T. Hughes, "Application of finite element modeling in LVDT design," *COMPEL*, vol. 11, no. 1, pp. 73–76, 1992

[18] M. Martino, A. Danisi, R. Losito, A. Masi, and G. Spiezia, "Design of a linear variable differential transformer with high rejection to external interfering magnetic field," IEEE Trans. on Magnetics, Vol. 46, No. 2, February 2010, pp. 674 - 677

[19] Alessandro Masi, Alessandro Danisi, Roberto Losito, Yves Perriard, "Characterization of magnetic immunity of an ironless inductive position sensor", *Sensors Journal IEEE*, vol. 13, no. 3, pp. 941-948, 2013

[20] Anish Babu, Boby George, "Design and development of a new non-contact inductive displacement sensor", *Sensors Journal IEEE*, vol. 18, no. 3, pp. 976-984, 2018.

[21] Narendiran Anandan, Boby George, "Design and development of a planar linear variable differential transformer for displacement sensing", *Sensors Journal IEEE*, vol. 17, no. 16, pp. 5298-5305, 2017.

[22] Adrian Grima, Alessandro Danisi, Alessandro Masi, Nicholas Sammut, "Influence of external conductive objects on the performance of an ironless inductive position sensor", *Sensors Journal IEEE*, vol. 17, no. 14, pp. 4500-4507, 2017.

[23] J. F. Gieras, "Analytical method of calculating the electromagnetic field and power losses in ferromagnetic halfspace, taking into account saturation and hysteresis", *Electrical Engineers, Proc. of the Institution of*, Year: 1977, Volume: 124, Pages: 1098 - 1104

[24] FEMM info, [Online].Available:http://www.femm.info/wiki/HomePage

[25] John David Jackson, Classical Electrodynamics, John Wiley & Sons, 1999

[26] Edmund E. Callaghan, Stephen H. Maslen, "The magnetic field of a finite solenoid," NASA, Oct 01, 1960, .)[Online]. Available:https://ntrs.nasa.gov/search.jsp?R=19980227402

[27] A. C. M. de Queiroz., "Mutual inductance and inductance calculations by Maxwell's method," .)[Online]. Available:http://www.coe.ufrj.br/~acmq/papers/papers.html